

A Closed-Form Formulation of HRBF-Based Surface Reconstruction

Shengjun Liu, Charlie C. L. Wang, *Senior Member, IEEE*, Guido Brunnert, and Jun Wang

Abstract—The *Hermite radial basis functions* (HRBFs) implicits have been used to reconstruct surfaces from scattered Hermite data points. In this work, we propose a closed-form formulation to construct HRBF-based implicits by a quasi-solution approximating the exact solution. A scheme is developed to automatically adjust the support sizes of basis functions to hold the error bound of a quasi-solution. Our method can generate an implicit function from positions and normals of scattered points without taking any global operation. Working together with an adaptive sampling algorithm, the HRBF-based implicits can also reconstruct surfaces from point clouds with non-uniformity and noises. Robust and efficient reconstruction has been observed in our experimental tests on real data captured from a variety of scenes.

Index Terms—Hermite Radial Basis Functions, Quasi-solution, Closed-Form, Surface Reconstruction

1 INTRODUCTION

RECONSTRUCTING surface from a set of unorganized points equipped with normal vectors is an important topic in various fields such as computer graphics, reverse engineering, image processing, mathematics, robotics and CAD/CAM. A lot of research approaches have been devoted to develop surface reconstruction methods, in which implicit surface fitting based on *Radial Basis Functions* (RBF) is successful in dealing with noisy and incomplete data (e.g., [1]–[3]).

Recently, implicits based on *Hermite Radial Basis Functions* (HRBF) were presented to interpolate data points to the first order [4]. It is robust and effective to deal with coarse and non-uniformly sampled points, close surface sheets, and surfaces with fine details. However, interpolating both positions and normals of points leads to the computation of solving a $4n \times 4n$ linear system for an input with n points. It is impractical due to the expensive computation. The system becomes sparse when the *Compactly Supported Radial Basis Functions* (CSRBF) are used as the kernel functions. However, this attempt on improving the efficiency can bring in a more challenging problem – numerical stability.

HRBF-based quasi-interpolation is presented in this paper to overcome the computational problem. Quasi-

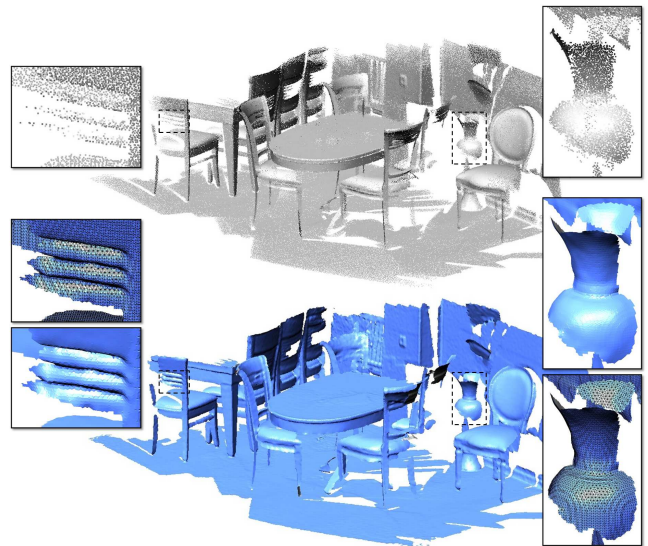


Fig. 1. The method proposed in this paper can efficiently reconstruct a surface from a set of noisy and incomplete points – e.g., the indoor scene shown here with 922k points. Our reconstruction takes only 60 seconds to generate a mesh surface that has the similar quality as the state-of-the-art [5] but the computation is $7.6\times$ faster. The parameter, $s = 3.5$, is employed in this reconstruction.

interpolation is a kind of approximate interpolation that fits implicits by weighted averages of the values at given points. The most attractive property of quasi-interpolation is to reconstruct a surface from a set of points without solving linear systems – i.e., with a closed-form formulation. This can make the computation of HRBF-based surface reconstruction stable and efficient. As shown in Fig.1, the mesh surface can be efficiently reconstructed from an input set with 922k points by our method in 60 seconds. Comparing to the

- S. Liu is with the School of Mathematics and Statistics, Central South University, Changsha 410083, China. E-mail: shjliu.cs@gmail.com
- C.C.L. Wang is with Department of Mechanical and Automation Engineering, The Chinese University of Hong Kong, Shatin, N.T., Hong Kong. Corresponding author - E-mail: cwang@mae.cuhk.edu.hk
- G. Brunnert is with Department of Computer Science, Chemnitz University of Technology, Chemnitz 09126, Germany.
- J. Wang is with the College of Mechanical and Electrical Engineering, Nanjing University of Aeronautics and Astronautics, Nanjing 210016, China.

recently published *Floating Scale Surface Reconstruction* (FSSR) that also avoids applying global operations, our method is about $7.6\times$ faster. $s = 3.5$ is the *only* parameter used in our approach. Here, s is defined as an amplifier of CSRBF kernels' support sizes, which control the maximal number of data points covered by each support (details can be found in Section 4.1). Moreover, we have analyzed the error-bound between our closed-form solution and the solution obtained by solving linear systems (see Section 3.2). Specifically, the error-bound exists when the number of points covered by the support of each kernel is capped by a fixed number. To overcome the problem caused by high non-uniformity on points, an algorithm is developed to select a sub-set of given points to serve as centers of kernel functions, which is an optional step in our framework of reconstruction.

1.1 Main result

In this paper, we propose a closed-form formulation for computing the quasi-solution of HRBF-based surface reconstruction from scattered data points.

- The method can construct a signed scalar function by directly blending the positions and normals of points without any global operation. The computation based on CSRBF is local and robust.
- Errors between the quasi-solution and the exact one are bounded after applying an automatical scheme to adjust the support sizes of basis functions.
- Combining with an adaptive center selection algorithm, surface reconstruction based on our method can remove the artifacts resulted from the non-uniformity and noises.

As a local approach, our method is efficient and scalable. This is well-suited for highly parallel implementation as well as distributed/progressive reconstruction. Note that, the compactly-supported basis functions results in open meshes and leaves holes in the region does not have enough number of points, which fits the application of reconstructing outdoor scenes very well.

1.2 Related work

The problem of surface reconstruction from point cloud has been studied in literature for more than two decades. A comprehensive review of all these works has beyond the scope of our paper. More discussion and comparison on different surface reconstruction methods can be found in [6]. We only give an overview of implicit function based reconstruction with a focus on RBF-based formulations.

After using signed distance field in [7] to reconstruct mesh surface from point clouds, implicit functions have gained a lot of attention in surface reconstruction because of its ability to handle topological change and fill holes. Example approaches

include RBF-based methods [1], [2], [4], [8]–[16], Poisson surface reconstructions [17], [18], smooth signed distance method [19], moving least-squares based methods [20]–[25], wavelets based method [26], and *Partition-Of-Unity* (POU) based methods [27], [28]. The methods based on RBF implicits are popular for their capability of handling sparse point clouds. Generally, RBF-based methods transform the reconstruction into a problem of multi-variational optimization, where enforcing the interpolation constraints results in a linear system. Solving the linear system is an important but time-consuming step for the RBF-based reconstruction. To obtain a non-trivial solution, RBF-based methods usually require the provision of extra offset-points (ref. [1], [2]) that can be obtained by shifting data points along their normal directions. However, it is not easy to find an optimal value for the offset scalar. The positions of these offset points is also difficult to determine, especially when the scanned model has thin sheets and the distribution of input points is irregular. To avoid generating offset-points, Ohtake et al. [9], [13] used a signed function which includes basic approximations and local details. The basic approximation formed by local quadratic functions with POU is considered as an offset function which constructs the non-zero constraints for fitting local details with RBFs. A very important information that describes shape to the first order – the normal vectors of a model have not been well utilized in these approaches of surface reconstruction.

Some prior works (e.g., [10], [15]) deduced from the statistical-learning perspective avoid generating offset-points in surface reconstruction, where normals were directly used in a variational formulation. Recently, Macedo et al. [4] derive an implicit function from the Hermite-Birkhoff interpolation with RBFs. They enhance the flexibility of HRBF reconstruction by ensuring well-posedness of an approach combining regularization. However, given a set with n points and n normal vectors, these methods give a $4n \times 4n$ linear system to be solved, which limits the number of points can be involved in the reconstruction.

Quasi-interpolation is a method in the field of function approximation. It is simple, efficient, and computational stable. In the early work of quasi-interpolation [29], a function approximating a given data set is defined by a weighted average of the values at the data points. The idea has been used in [30] for surface reconstruction. The quasi-interpolation with radial basis functions has been studied in [31]. Recently, Wu and Xiong [32] developed a new method to construct kernels in a quasi-interpolation scheme by the linear combination of scales, where the kernels are in the form of RBF. Han and Hou discussed quasi-interpolation by RBF and suggested values of the shape parameters in [33], which is a constructive method for obtaining a family of quasi-interpolations. Liu and Wang generalized the regularly sampled grid

points to 3D scattered points in [34]. They proposed a multi-level quasi-interpolation method which is based on POU and the RBF method. However, linear systems still need to be solved in their method. Locally supported basis functions satisfying the property of POU are used in the recent work FSSR [5], in which weighted average is employed to fit implicit functions to the input set of points. However, there is no error-bound guaranteed in their approach. Experimental tests show that our method can generate results with similar quality as FSSR but has 7.61 to 98.3 times speedup.

There are schemes for finding a subset of ‘optimal’ centers from the point set in order to obtain fast reconstructions. Carr et al. [1] proposed a greedy algorithm that iteratively appends centers which are corresponding to the maximal residual of the current RBF fitting until a desired accuracy is reached. Samozino *et al.* presented the reconstruction with voronoi centered RBFs [11]. Ohtake et al. [13] proposed a reconstruction method which combines an adaptive POU approximation with least-squares RBF fitting. Different from [13], we adopt a quadric error function based on positions and normals of a point and its neighbors instead of local quadratic approximation. Therefore, our center selection step can generate a good spherical cover in a non-iterative way. The selected centers of spheres describe the input shape with a small error.

The rest of our paper is organized as follows. We first introduce the surface reconstruction based on regularized HRBF implicits in Section 2. Section 3 provides our formulation in the closed-form and derives the error bound of our formulation. Section 4 presents the algorithms for different steps of reconstruction, including parameters tuning, isosurface extraction and center selection (optional). After that, the results of experimental tests are shown and discussed in Section 5. Lastly, our paper ends with the conclusion.

2 HRBF IMPLICITS

The HRBF implicits [4] are built upon the theory of Hermite-Birkhoff interpolation with radial basis functions [3]. In this section, we briefly describe how to use HRBF implicits to solve the problem of surface reconstruction from scattered points.

Definition 1 Given a set of data $\mathcal{P} = \{\mathbf{p}_1, \mathbf{p}_2, \dots, \mathbf{p}_n\}$ with unit normals $\mathcal{N} = \{\mathbf{n}_1, \mathbf{n}_2, \dots, \mathbf{n}_n\}$, the HRBF implicits give a function f interpolating both the points and the normal vectors as

$$f(\mathbf{x}) = \sum_{j=1}^n \{a_j \varphi(\mathbf{x} - \mathbf{p}_j) - \langle \mathbf{b}_j, \nabla \varphi(\mathbf{x} - \mathbf{p}_j) \rangle\}, \quad (1)$$

where $\varphi: \mathbb{R}^3 \mapsto \mathbb{R}$ is defined by a radial basis function $\varphi(\mathbf{x}) = \phi_\rho(\|\mathbf{x}\|)$, $\langle \cdot, \cdot \rangle$ denotes the dot-product of two vectors, and ∇ is the gradient operator.

The scalar coefficients, $a_j \in \mathbb{R}$, and the vector coefficients, $\mathbf{b}_j \in \mathbb{R}^3$, can be determined by the constraints of interpolation as

$$f(\mathbf{p}_i) = c \text{ and } \nabla f(\mathbf{p}_i) = \mathbf{n}_i, \quad (i = 1, 2, \dots, n) \quad (2)$$

with c being a constant value for the implicit function. $c = 0$ is used for surface reconstruction. Applying the constraints (2) to Eq.(1), we obtain a linear system with equations

$$\begin{aligned} \sum_{j=1}^n \{a_j \varphi(\mathbf{p}_i - \mathbf{p}_j) - \langle \mathbf{b}_j, \nabla \varphi(\mathbf{p}_i - \mathbf{p}_j) \rangle\} &= c, \\ \sum_{j=1}^n \{a_j \nabla \varphi(\mathbf{p}_i - \mathbf{p}_j) - \mathbf{b}_j \mathbf{H} \varphi(\mathbf{p}_i - \mathbf{p}_j)\} &= \mathbf{n}_i, \end{aligned} \quad (3)$$

where $i = 1, 2, \dots, n$ and \mathbf{H} is the Hessian operator applied on $\varphi(\cdot)$. The linear system can be rewritten in a matrix form as

$$\mathbf{A} \boldsymbol{\lambda} = \mathbf{y}, \quad (4)$$

where $\boldsymbol{\lambda}$ and \mathbf{y} are $4n$ vectors with the i -th blocks being $[a_i, \mathbf{b}_i]^T$ and $[c, \mathbf{n}_i]^T$ respectively. Here, \mathbf{A} is a $4n \times 4n$ coefficients matrix which are assembled from $n \times n$ blocks. Each block $\mathbf{A}_{i,j}$ is a 4×4 sub-matrix corresponding to a pair of RBF centers $(\mathbf{p}_i, \mathbf{p}_j)$.

$$\begin{aligned} \mathbf{A} &= (\mathbf{A}_{i,j})_{n \times n}, \\ \mathbf{A}_{i,j} &= \begin{pmatrix} \varphi(\mathbf{p}_i - \mathbf{p}_j) & -\nabla \varphi(\mathbf{p}_i - \mathbf{p}_j) \\ \nabla \varphi(\mathbf{p}_i - \mathbf{p}_j) & -\mathbf{H} \varphi(\mathbf{p}_i - \mathbf{p}_j) \end{pmatrix}_{4 \times 4}. \end{aligned} \quad (5)$$

In this paper, we use a Wendland’s CSRBF [35] as the kernel function

$$\begin{aligned} \phi_\rho(r) &= \phi(r/\rho) \\ \phi(t) &= \begin{cases} (1-t)^4(4t+1), & t \in [0, 1], \\ 0, & \text{otherwise,} \end{cases} \end{aligned} \quad (6)$$

where ρ is the support size, and r is the Euclidean distance between a query point and the center of a RBF. Note that, different support sizes can be used at different centers. Solving Eq.(4), an implicit function $f(\mathbf{x})$ can be determined at the space spanned by the supports of centers $\{\mathbf{p}_i\}$. To make the system matrix of RBF interpolation better conditioned, a regularization term with coefficient η is usually added when using RBF interpolants to solve the surface reconstruction problem (ref. [36]). That is,

$$(\mathbf{A} + \eta \mathbf{I}) \boldsymbol{\lambda} = \mathbf{y}. \quad (7)$$

An example is shown in Fig.2 to demonstrate the effectiveness of regularization.

3 FORMULATION

This section provides a closed-form formulation for solving the HRBF-based surface reconstruction problem via quasi-solution. Error-bound of the approximation is also derived.

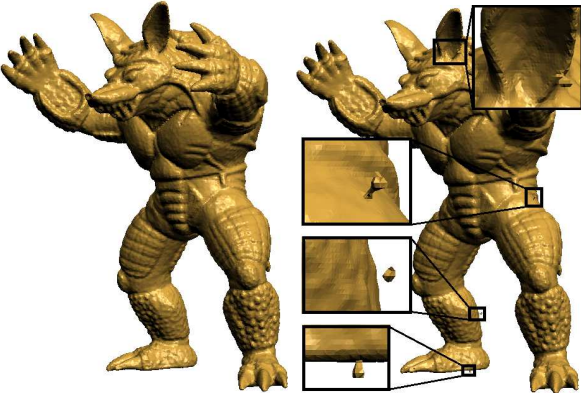


Fig. 2. Surface reconstructions by the HRBF implicits with (left) and without (right) the regularization term. Artifacts will be produced when the regularization term is *not* added. In this example, $\eta = 100/\rho^2$ is employed.

3.1 Quasi-solution in closed-form

When increasing the number of centers in the linear system of HRBF-based surface reconstruction (i.e., Eq.(7)), numerical instability and expensive computation become intensively remarkable. Here, we investigate a closed-form formulation derived from the theorem of quasi-interpolation to reconstruct surface in a more stable and efficient way.

Quasi-interpolation technique can reconstruct a function interpolating a given data set by computing weighted averages of the values at the data points [29]. Specifically, considering an exact interpolant $g(\mathbf{x}) = \sum_i \lambda_i \psi_i(\mathbf{x})$ with the constraints $g(\mathbf{x}_i) = f_i$ of function values, the function $g(\mathbf{x})$ can be well approximated by letting $\lambda_i \equiv f_i$. That is a quasi-interpolation, $\tilde{g}(\mathbf{x}) = \sum_i f_i \psi_i(\mathbf{x})$. However, the quasi-interpolation technique cannot be directly applied here as our interpolation constraints consist of both the values and the gradients of functions (see Eq.(2)).

Basically, we need a closed-form formulation to approximate the solution of Eq.(7). By means of the matrix computation, the quasi-interpolant with $\lambda_i \equiv f_i$ is actually a quasi-solution when the coefficient matrix is approximated by an identity matrix \mathbf{I} . Here, a similar approximation is employed in the HRBF-based reconstruction problem. For a CSRBF $\varphi_i(\dots)$, when there is no other center falling into the space spanned by its support ρ_i , the coefficient matrix is degenerated from $\mathbf{A}_{i,i}$ of Eq.(5) into

$$\mathbf{D}_{i,i} = \text{diag}\left(1, \frac{20}{\rho_i^2}, \frac{20}{\rho_i^2}, \frac{20}{\rho_i^2}\right) + \eta \mathbf{I}_4, \quad \mathbf{D}_{i,j} = 0 \quad (i \neq j). \quad (8)$$

If the scenario of not containing other centers happens at all CSRBF kernels, the linear system to be solved in Eq.(7) is degenerated into $\mathbf{D}\boldsymbol{\lambda} = \mathbf{y}$ with $\mathbf{D} = (\mathbf{D}_{i,j})_{n \times n}$. This leads to an approximate solution

of Eq.(7) as

$$\begin{aligned} \tilde{\boldsymbol{\lambda}} &= \mathbf{D}^{-1}\mathbf{y} \\ &= \left\{ \frac{c}{1+\eta}, \frac{\rho_1^2 \mathbf{n}_1}{20+\eta\rho_1^2}, \dots, \frac{c}{1+\eta}, \frac{\rho_n^2 \mathbf{n}_n}{20+\eta\rho_n^2} \right\}. \end{aligned} \quad (9)$$

The zero level-set is usually employed in surface reconstruction (i.e., $c = 0$ in Eqs.(2) and (3)). $c = 0$ is used in all formulas in the rest of this paper. As a result, the coefficients of the i -th basis function can be approximated by

$$a_i \approx 0 \quad \text{and} \quad \mathbf{b}_i \approx \frac{\rho_i^2}{20 + \eta\rho_i^2} \mathbf{n}_i,$$

which give an approximate function of $f(\mathbf{x})$ in a closed form as

$$\tilde{f}(\mathbf{x}) = - \sum_{j=1}^n \left\langle \frac{\rho_j^2}{20 + \eta\rho_j^2} \mathbf{n}_j, \nabla\varphi(\mathbf{x} - \mathbf{p}_j) \right\rangle. \quad (10)$$

By this implicit function, we can apply the polygonization techniques (e.g., [37], [38]) to tessellate the isosurface of $f(\mathbf{x}) = 0$ into a polygonal mesh – the surface is reconstructed from scattered Hermite points.

3.2 Error-bound analysis

The error between the quasi-solution $\tilde{\boldsymbol{\lambda}}$ and the exact solution $\boldsymbol{\lambda}$ of Eq.(7) must be bounded to make the closed-form formulation useful. The analysis is given below.

Lemma 1 Defining $\Delta\mathbf{A} = (\mathbf{A} + \eta\mathbf{I}) - \mathbf{D}$ and $\Delta\boldsymbol{\lambda} = \boldsymbol{\lambda} - \tilde{\boldsymbol{\lambda}}$, the error of approximation is bounded as

$$\|\Delta\boldsymbol{\lambda}\|_\infty \leq \frac{\|\mathbf{D}^{-1}\|_\infty \|\Delta\mathbf{A}\|_\infty}{1 - \|\mathbf{D}^{-1}\|_\infty \|\Delta\mathbf{A}\|_\infty} \|\mathbf{D}^{-1}\mathbf{y}\|_\infty \quad (11)$$

when $\|\mathbf{D}^{-1}\|_\infty \|\Delta\mathbf{A}\|_\infty < 1$.

Proof: By Eq.(7), we have

$$(\mathbf{D} + \Delta\mathbf{A})(\tilde{\boldsymbol{\lambda}} + \Delta\boldsymbol{\lambda}) = \mathbf{y}.$$

With the quasi-solution that $\tilde{\boldsymbol{\lambda}} = \mathbf{D}^{-1}\mathbf{y}$, this equation can be converted to

$$\Delta\boldsymbol{\lambda} = \mathbf{D}^{-1}[-(\Delta\mathbf{A})\tilde{\boldsymbol{\lambda}} - (\Delta\mathbf{A})(\Delta\boldsymbol{\lambda})].$$

Then, we apply a maximum norm and get

$$\|\Delta\boldsymbol{\lambda}\|_\infty \leq \|\mathbf{D}^{-1}\|_\infty (\|\Delta\mathbf{A}\|_\infty \|\tilde{\boldsymbol{\lambda}}\|_\infty + \|\Delta\mathbf{A}\|_\infty \|\Delta\boldsymbol{\lambda}\|_\infty),$$

which is also

$$(1 - \|\mathbf{D}^{-1}\|_\infty \|\Delta\mathbf{A}\|_\infty) \|\Delta\boldsymbol{\lambda}\|_\infty \leq \|\mathbf{D}^{-1}\|_\infty \|\Delta\mathbf{A}\|_\infty \|\tilde{\boldsymbol{\lambda}}\|_\infty.$$

By the given condition $\|\mathbf{D}^{-1}\|_\infty \|\Delta\mathbf{A}\|_\infty < 1$, we have

$$\|\Delta\boldsymbol{\lambda}\|_\infty \leq \frac{\|\mathbf{D}^{-1}\|_\infty \|\Delta\mathbf{A}\|_\infty}{1 - \|\mathbf{D}^{-1}\|_\infty \|\Delta\mathbf{A}\|_\infty} \|\tilde{\boldsymbol{\lambda}}\|_\infty.$$

Combining with Eq.(9), the lemma has been proved. ■

Assuming there are at most m other centers falling in the support region for each kernel, the error-bound of our quasi-solution can be achieved on the Wendland's CSRBFs (i.e., Eq.(6)).

Lemma 2 When Wendland's CSRBFs are used, if their support sizes $\rho_i \in [\rho_{\min}, \rho_{\max}]$ (with $\rho_{\max} < \sqrt{20}$) and each support region contains at most m centers of other CSRBFs, the error of $\|\Delta\lambda\|_\infty$ is bounded by a constant when

$$\eta > \left(m \left(\frac{5}{4\rho_{\min}} + \frac{35}{\rho_{\min}^2} \right) - 1 \right). \quad (12)$$

Proof: By the definition of the diagonal matrix \mathbf{D} in Eq.(8),

$$\|\mathbf{D}^{-1}\|_\infty = \max_{j=1, \dots, n} \left\{ \frac{1}{1+\eta}, \frac{\rho_j^2}{20+\eta\rho_j^2} \right\}.$$

The upper bound of $\|\mathbf{D}^{-1}\mathbf{y}\|_\infty$ can also be obtained from Eq.(9) as

$$\begin{aligned} \|\mathbf{D}^{-1}\mathbf{y}\|_\infty &= \|\tilde{\lambda}\|_\infty \\ &= \max_{j=1, \dots, n} \left\{ 0, \frac{\rho_j^2 \mathbf{n}_j^x}{20+\eta\rho_j^2}, \frac{\rho_j^2 \mathbf{n}_j^y}{20+\eta\rho_j^2}, \frac{\rho_j^2 \mathbf{n}_j^z}{20+\eta\rho_j^2} \right\}. \end{aligned}$$

Here, superscripts denote the x -, y - and z -components of a vector in \mathbb{R}^3 . When $\rho_i > \rho_j > 0$ and $\eta \geq 0$,

$$\frac{\rho_i^2}{20+\eta\rho_i^2} = \frac{1}{20/\rho_i^2 + \eta} > \frac{\rho_j^2}{20+\eta\rho_j^2} = \frac{1}{20/\rho_j^2 + \eta}.$$

As a result

$$\begin{aligned} \|\mathbf{D}^{-1}\|_\infty &\leq \max\left(\frac{1}{1+\eta}, \frac{\rho_{\max}^2}{20+\eta\rho_{\max}^2}\right) \\ \|\mathbf{D}^{-1}\mathbf{y}\|_\infty &\leq \frac{\rho_{\max}^2}{20+\eta\rho_{\max}^2}. \end{aligned}$$

When $\rho_j \leq \rho_{\max} < \sqrt{20}$, we can further obtain

$$\|\mathbf{D}^{-1}\|_\infty = \frac{1}{1+\eta}.$$

Now we derive the upper bound of $\|\Delta\mathbf{A}\|_\infty$. From Eqs.(5) and (8), using $\varphi_{i,j}$ to denote $\varphi_i(\mathbf{p}_j) = \varphi(\mathbf{p}_j - \mathbf{p}_i)$, we can also have

$$\begin{aligned} \|\Delta\mathbf{A}\|_\infty &= \max_{j=1, \dots, n} \left\{ \right. \\ &\sum_i^m (|\varphi_{i,j}| + |\frac{\partial\varphi_{i,j}}{\partial x}| + |\frac{\partial\varphi_{i,j}}{\partial y}| + |\frac{\partial\varphi_{i,j}}{\partial z}|), \\ &\sum_i^m (|\frac{\partial\varphi_{i,j}}{\partial x}| + |\frac{\partial^2\varphi_{i,j}}{\partial x^2}| + |\frac{\partial^2\varphi_{i,j}}{\partial x\partial y}| + |\frac{\partial^2\varphi_{i,j}}{\partial x\partial z}|), \\ &\sum_i^m (|\frac{\partial\varphi_{i,j}}{\partial y}| + |\frac{\partial^2\varphi_{i,j}}{\partial x\partial y}| + |\frac{\partial^2\varphi_{i,j}}{\partial y^2}| + |\frac{\partial^2\varphi_{i,j}}{\partial y\partial z}|), \\ &\left. \sum_i^m (|\frac{\partial\varphi_{i,j}}{\partial z}| + |\frac{\partial^2\varphi_{i,j}}{\partial x\partial z}| + |\frac{\partial^2\varphi_{i,j}}{\partial y\partial z}| + |\frac{\partial^2\varphi_{i,j}}{\partial z^2}|) \right\}. \end{aligned}$$

TABLE 1
Derivatives of Wendland's CSRBF [35]

$\varphi_i(\mathbf{x})$	$(1 - \frac{r}{\rho_i})^4 (4\frac{r}{\rho_i} + 1)$
$\frac{\partial\varphi_i(\mathbf{x})}{\partial x}$	$-\frac{20}{\rho_i^2} (1 - \frac{r}{\rho_i})^3 (x - x_i)$
$\frac{\partial\varphi_i(\mathbf{x})}{\partial y}$	$-\frac{20}{\rho_i^2} (1 - \frac{r}{\rho_i})^3 (y - y_i)$
$\frac{\partial\varphi_i(\mathbf{x})}{\partial z}$	$-\frac{20}{\rho_i^2} (1 - \frac{r}{\rho_i})^3 (z - z_i)$
$\frac{\partial^2\varphi_i(\mathbf{x})}{\partial x^2}$	$-\frac{20}{\rho_i^2} (1 - \frac{r}{\rho_i})^3 + \frac{60}{\rho_i^3} (1 - \frac{r}{\rho_i})^2 \frac{(x - x_i)^2}{r}$
$\frac{\partial^2\varphi_i(\mathbf{x})}{\partial y^2}$	$-\frac{20}{\rho_i^2} (1 - \frac{r}{\rho_i})^3 + \frac{60}{\rho_i^3} (1 - \frac{r}{\rho_i})^2 \frac{(y - y_i)^2}{r}$
$\frac{\partial^2\varphi_i(\mathbf{x})}{\partial z^2}$	$-\frac{20}{\rho_i^2} (1 - \frac{r}{\rho_i})^3 + \frac{60}{\rho_i^3} (1 - \frac{r}{\rho_i})^2 \frac{(z - z_i)^2}{r}$
$\frac{\partial^2\varphi_i(\mathbf{x})}{\partial x\partial y}$	$\frac{60}{\rho_i^3} (1 - \frac{r}{\rho_i})^2 \frac{(x - x_i)(y - y_i)}{r}$
$\frac{\partial^2\varphi_i(\mathbf{x})}{\partial x\partial z}$	$\frac{60}{\rho_i^3} (1 - \frac{r}{\rho_i})^2 \frac{(x - x_i)(z - z_i)}{r}$
$\frac{\partial^2\varphi_i(\mathbf{x})}{\partial y\partial z}$	$\frac{60}{\rho_i^3} (1 - \frac{r}{\rho_i})^2 \frac{(y - y_i)(z - z_i)}{r}$

[†]Here, $\mathbf{x} = (x, y, z)$, $r = \sqrt{(x - x_i)^2 + (y - y_i)^2 + (z - z_i)^2}$ and ρ_i is the support size of the radial basis function $\varphi_i(\mathbf{x})$.

By the derivatives listed in Table 1 and their corresponding upper bounds listed in Table 2, we can have

$$\begin{aligned} \|\Delta\mathbf{A}\|_\infty &\leq \max_j \left\{ m \left(1 + \frac{15}{4\rho_j} \right), m \left(\frac{5}{4\rho_j} + \frac{35}{\rho_j^2} \right) \right\} \\ &\leq \max \left\{ m \left(1 + \frac{15}{4\rho_{\min}} \right), m \left(\frac{5}{4\rho_{\min}} + \frac{35}{\rho_{\min}^2} \right) \right\}. \end{aligned}$$

When $\rho_{\min} \leq \rho_{\max} < \sqrt{20}$, it can easily be further simplified to

$$\|\Delta\mathbf{A}\|_\infty \leq m \left(\frac{5}{4\rho_{\min}} + \frac{35}{\rho_{\min}^2} \right) \equiv \bar{A}.$$

Summarizing all the analysis together, we have

$$\|\Delta\lambda\|_\infty \leq \frac{\bar{A}\rho_{\max}^2}{(1+\eta-\bar{A})(20+\eta\rho_{\max}^2)} \quad (13)$$

when $\|\mathbf{D}^{-1}\|_\infty \|\Delta\mathbf{A}\|_\infty \leq \bar{A}/(1+\eta) < 1$. To hold this, it should have $1+\eta > \bar{A}$ – that is Eq.(12). The lemma has been proved. \blacksquare

Remark. The requirements of,

- 1) all the CSRBFs have their support sizes within the interval $[\rho_{\min}, \rho_{\max}]$, and
- 2) there are at most m centers falling in the support of any others CSRBF,

can be achieved by a carefully designed parameter tuning algorithm (see Section 4.1). After determining the support sizes, the value of η can be chosen to hold Eq.(12). By scaling all models into a bounding box of

TABLE 2
Error Bounds of Derivatives

$ \varphi_i(\mathbf{x}) $	≤ 1
$ \frac{\partial \varphi_i(\mathbf{x})}{\partial x} , \frac{\partial \varphi_i(\mathbf{x})}{\partial y} , \frac{\partial \varphi_i(\mathbf{x})}{\partial z} $	$\leq \frac{20}{\rho_i} (1 - \frac{r}{\rho_i})^3 \frac{r}{\rho_i}$ $\leq \frac{5}{4\rho_i^2}$ (with $r = \frac{\rho_i}{2}$)
$ \frac{\partial^2 \varphi_i(\mathbf{x})}{\partial x^2} , \frac{\partial^2 \varphi_i(\mathbf{x})}{\partial y^2} , \frac{\partial^2 \varphi_i(\mathbf{x})}{\partial z^2} $	$\leq \frac{20}{\rho_i^2} (1 - \frac{r}{\rho_i})^2 (1 + 2\frac{r}{\rho_i})$ $\leq \frac{20}{\rho_i^2}$ (with $r = 0$)
$ \frac{\partial^2 \varphi_i(\mathbf{x})}{\partial x \partial y} , \frac{\partial^2 \varphi_i(\mathbf{x})}{\partial x \partial z} , \frac{\partial^2 \varphi_i(\mathbf{x})}{\partial y \partial z} $	$\leq \frac{60}{\rho_i^2} (1 - \frac{r}{\rho_i})^2 \frac{r}{\rho_i}$ $\leq \frac{15}{2\rho_i^2}$ (with $r = \frac{\rho_i}{2}$)

‡The analysis is based on $|x - x_i| \leq r, |y - y_i| \leq r$ and $|z - z_i| \leq r$, and the bound is derived by using the inequality of arithmetic and geometric means.

$[-1, 1]^3 \in \mathbb{R}^3$, the algorithm in Section 4.1 can also enforce $\rho_{\max} < \sqrt{20}$. Numerical errors generated in our experimental tests are discussed in Section 5.3, which further verify the error-bound of our method.

4 RECONSTRUCTION ALGORITHM

Given points and their normals in the input sets \mathcal{P} and \mathcal{N} , the implicit function $\tilde{f}(\mathbf{x})$ defined in Eq.(10) can be evaluated in the supported regions as an approximation of the HRBF reconstruction. Specifically, with the help of tessellation techniques, zero isosurface of the implicit function $\tilde{f}(\mathbf{x})$ can be converted into a mesh surface. A scheme is also developed to determine the support sizes of HRBFs and the coefficient η according to Lemma 2 to guarantee the existence of error-bound.

Our reconstruction algorithm consists of a scheme to tune parameters according to the analysis for error-bound and an efficient method akin to DC to extract the zero isosurface as a polygonal mesh in the supported regions of $\tilde{f}(\mathbf{x})$. When processing highly non-uniform point sets, an optional step of center selection is needed to reduce the artifacts caused by the non-uniformity. After that, the input sets \mathcal{P} and \mathcal{N} are reduced into a set $\mathcal{C} = \{c_1, \mathbf{n}_1, \dots, c_l, \mathbf{n}_l\}$ with less Hermite points (i.e., $l < n$).

4.1 Parameters tuning

The support sizes of HRBF implicits, $\rho_j s$, and the coefficient of regularization, η , should satisfy the condition in Eq.(12) for the existence of error-bound. Specifically, the following factors must be considered:

- $\rho_{\max} = \max\{\rho_j\} < \sqrt{20}$ gives the upper bounds of ρ_j .
- According to Eq.(12), with larger ρ_{\min} , users will have more flexibility to choose the value of η (i.e.,

has smaller value for the right of the inequality in Eq.(12)).

- On the other aspect, if increasing the support size ρ_j of a RBF centered at \mathbf{p}_j , more other centers will be covered by the supporting region. This increases the value of m in Lemma 2 and thus the right-hand side of the inequality in Eq.(12).

Based on these reasons, we develop a scheme below to determine the values of $\rho_j s$ and η .

Each support must cover enough number of data points to generate a span of the local shape; meanwhile, it cannot be too large. For this purpose, we first construct an octree to split the input points into different nodes by keeping similar number of points in each leaf-nodes. \bar{d} is then set as 3/4 of the average diagonal length of the leaf-nodes. The support sizes are temporally set as $s\bar{d}$ with s being an amplifier – $s = 1.0$ is employed for clean data sets. We then count the number of points covered by the supporting region of each CSRBF, $\phi_{\rho_j}(\|\mathbf{x} - \mathbf{p}_j\|)$. The value of m is selected as the maximal number of data points covered by each of these temporary supports. After determining the value of m , ρ_j of each CSRBF is enlarged by an incremental procedure until the support contains more than m points. By the fixed support sizes, the value of η can be chosen by Eq.(12). In all our tests, we assign it with a value slightly larger (e.g., 10^{-5}) than the right-hand side of Eq.(12).

The values of $\rho_j s$ determined by the above method work well on clean data but may fail in highly noisy input. Further tuning is needed. First of all, we enlarge the temporal support sizes by using $s > 1.0$ to enhance the effectiveness of denoising. This results in a larger m . More geometric details can be preserved with a smaller support size while a larger support size leads to a smoother reconstruction. Moreover, among all the $\rho_j s$ obtained by the aforementioned method, the minimal value of $\rho_j s$ is selected as the final support size for all CSRBF kernels – i.e., uniform support size is adopted for highly noisy input. Examples using different amplifiers can be found in Fig.3.

4.2 Efficient isosurface extraction

Our surface reconstruction method only evaluates the function values of the implicit function $\tilde{f}(\mathbf{x})$ during the isosurface extraction step. An variation of DC algorithm [38] is developed to extract zero isosurfaces from the regions spanned by the RBFs in Eq.(10). In our method, the reconstruction with compactly supported implicit functions leads to open mesh surfaces and leaves holes in regions not covered by the supports of RBFs. This is very useful for reconstructing the scenes that have not been completely captured (e.g., the scene shown in Fig.1). Moreover, as $\tilde{f}(\mathbf{x})$ is defined in a closed-form, the function evaluation (therefore also the isosurface extraction) is highly

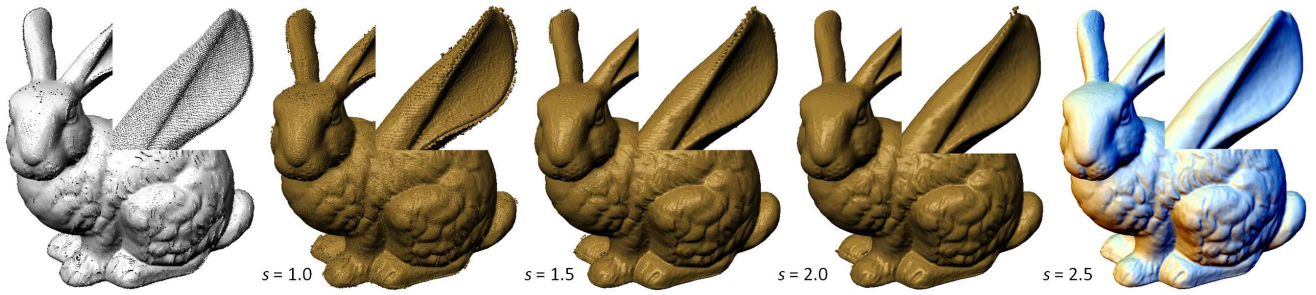


Fig. 3. Results with different regularization can be obtained by using different amplifiers on a noisy point set: (from left to right) input noisy points and our reconstruction results. In these examples, η is chosen as a value slightly greater than the right of Eq.(12).

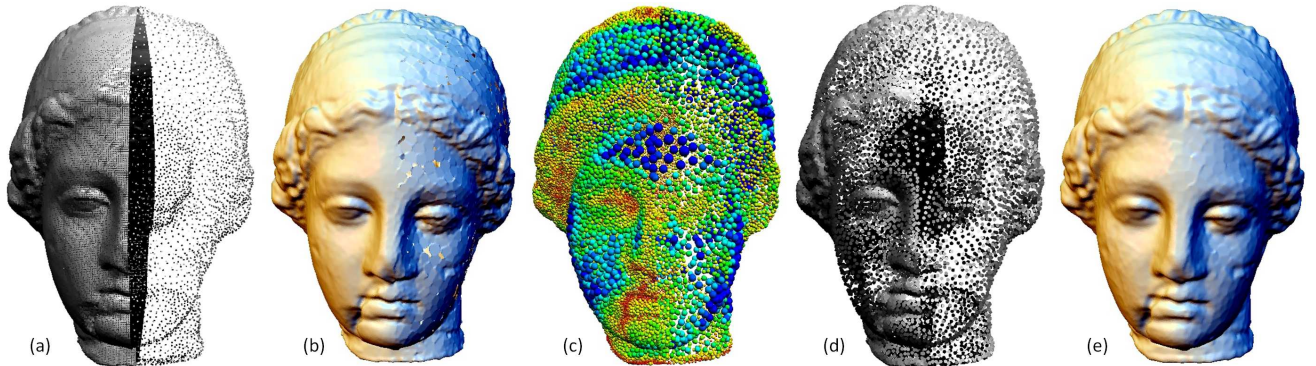


Fig. 4. Adaptive HRBF implicits are generated by our method with the help of center selection: (a) the input set with 100,371 points in high non-uniformity, (b) the reconstruction using all points as centers of HRBF implicits will easily lead to holes in the sparse regions, (c) the spherical cover – the spheres are displayed in radii as 1/4 of the real ones, (d) the selected 13,446 centers of RBFs, and (e) reconstruction from the selected centers – no hole will be generated as the densities of centers in the left and the right are similar to each other. The support sizes are determined by the method in Section 4.1 with (b) $s = 2.1$ and (e) $s = 1.0$, both of which lead to $m = 120$.

scalable and can be efficiently performed by local operations.

Voxels with a fixed width w are constructed and those intersecting the isosurface $\tilde{f}(\mathbf{x}) = 0$ are first searched in the supported regions around the centers $\{\mathbf{p}_j\}$. The voxels are constructed only when 1) all of its eight corners have function values *defined* and 2) the function values have *different signs*. For each edge e of a voxel, the intersection between e and the isosurface can be determined by a bi-sectional search when two endpoints of e have different signs in $\tilde{f}(\cdot)$. The normal of this intersection point is assigned as $\nabla\tilde{f}$. For each voxel, a vertex is constructed at the position \mathbf{v} that minimize the quadratic-function $\sum_j ((\mathbf{v} - \mathbf{q}_j) \cdot \mathbf{n}_{q_j})^2$, where \mathbf{q}_j and \mathbf{n}_{q_j} are the intersection points on edges and the normal vectors at the intersections. For each edge e with intersection, a quadrangle is constructed by linking the vertices in the four voxels around e . As a result, the final surface mesh can be obtained.

In our current implementation, the mesh surface is extracted from voxels with a fixed width. More sophisticated algorithm can be developed to construct an octree based hierarchy to extract triangles adaptively on a partial region of implicit surfaces (e.g., [39]). All the operations in our isosurface evaluation

and extraction steps are local. It is easy to be implemented in parallel on many-cores or in a distributed environment. By the algorithm’s locality, a progressive reconstruction can be easily developed by only updating a local region when new points (as centers of CSRBFs) are added.

4.3 Center selection

This is an optimal step to be applied when high non-uniformity is observed on the input points. For such a point set, the direct reconstruction by using all points as centers of CSRBFs results in a reconstruction with holes in the sparse regions (see Fig.4(b) for an example). Here, we adaptively select samples from \mathcal{P} and \mathcal{N} to form a subset \mathcal{C} . The Hermite points in \mathcal{C} will be used as centers of HRBF in the above method to obtain a better surface reconstruction. Each center, \mathbf{c}_k , is also associated with a radius, r_k , which therefore forms a local spherical cover of the given points.

Definition 2 The *degree of coverage* (DoC) at a point $\mathbf{x} \in \mathbb{R}^3$ is defined as a function

$$g(\mathbf{x}) = \sum_{k=1}^l \phi_{r_k}(\|\mathbf{x} - \mathbf{c}_k\|) \quad (14)$$

according to a set of down-sampled Hermite points, $\mathcal{C} = \{\mathbf{c}_1, \mathbf{n}_1, \dots, \mathbf{c}_l, \mathbf{n}_l\}$.

We wish to generate a minimal spherical cover by controlling DoC in an iterative procedure.

The basic idea of center selection is to form spherical covers by letting DoC at every point in \mathcal{P} not less than a criterion g_{\min} (i.e., $\forall \mathbf{p}_j \in \mathcal{P}, g(\mathbf{p}_j) \geq g_{\min}$). To this end, the following steps are iteratively run until the criterion is satisfied at all points.

- 1) In the initial step, $\mathcal{C} = \emptyset$ and $g_j = 0$ is assigned to all points $\mathbf{p}_j \in \mathcal{P}$.
- 2) Randomly selecting ϖ points with their DoCs less than g_{\min} . Among these ϖ points, the point with the smallest $g(\cdot)$ is chosen as a center \mathbf{c}_k to add into \mathcal{C} together with its normal vector.
- 3) The radius r_k of sphere centered at \mathbf{c}_k is then determined by a quadric-error function

$$q(\mathbf{c}_k, r_k) = \frac{\sum_j \delta_j \phi_{r_k}(\|\mathbf{p}_j - \mathbf{c}_k\|)(\mathbf{n}_j \cdot (\mathbf{c}_k - \mathbf{p}_j))^2}{\sum_j \delta_j \phi_{r_k}(\|\mathbf{p}_j - \mathbf{c}_k\|)},$$

which evaluates how curved the surface inside the sphere is – the shape is represented by sample points in \mathcal{P} . In other words, for a highly curved region, a sphere with smaller r_k should be used to reduce the error. Here, δ_j is the average of the squared distances between a point \mathbf{p}_j and its 15 nearest neighboring points. The value of δ_j indicates a weight of point density. The bisectional search is taken to obtain a maximal r_k that still satisfies

$$q(\mathbf{c}_k, r_k) \leq q_{err} \bar{L}$$

with \bar{L} being the diagonal length of the input points' bounding box.

- 4) Updating DoC at all points \mathbf{p}_j within the range $\|\mathbf{p}_j - \mathbf{c}_k\| < r_k$ while $g(\mathbf{p}_j) < g_{\min}$. DoC of \mathbf{c}_k is assigned as g_{\min} to avoid being selected as candidates of centers once again.
- 5) Go back to step 2) until DoC at all points are not less than g_{\min} .

Note that, this iterative procedure is a variant of our prior work in [40] with certain modification to fit the formulation of CSRBF. The efficiency of computation has also been improved. An example result of our minimal spherical covering is shown in Fig.4(c), where the selected centers of RBFs are displayed as spheres. Colors are used to represent the sizes of spheres with red for the smallest and blue for the biggest ones. Samples adaptive to the geometric details have been illustrated as Fig.4(d). In all examples of this paper, $g_{\min} = 1.5$, $q_{err} = 5 \times 10^{-4}$ and $\varpi = 15$ work well.

With the centers selected above, a reduced implicit function can be obtained by Eq.(10) but with fewer centers of CSRBFs. After applying the center selection step, the density of centers at each region becomes compatible to its neighboring regions – i.e., no sharp

change. As a result, a better reconstruction can be obtained (see the result shown in Fig.4(e)).

5 RESULTS AND DISCUSSION

An surface reconstruction algorithm based on the closed-form formulation of HRBF implicits has been implemented with Microsoft Visual C++ and OpenGL. We evaluate our methods on a PC with two Intel Core i7-2600K CPUs at 3.4GHz plus 16GB RAM. Our approach has been applied to various data with up to fourteen millions of points (the surface can be reconstructed in 78.9 sec.). Our results are compared with a variety of approaches – see the examples and discussions presented below. All the models are re-scaled into a bounding-box of $[-1, 1]^3 \in \mathbb{R}^3$.

5.1 Comparisons

Firstly, we test the performance of our approach on sets of clean points, which are uniformly sampled from polygonal meshes. Four models, Ramesses, Raptor, Momento and Neptune, are sampled into sets with $0.58M \sim 4.98M$ points. Our results are compared with three prior methods, including the *Multiple Partition of Unity* (MPU) reconstruction [28], the *Smooth Signed Distance* (SSD) reconstruction [19] and the *Screened-Poisson* reconstruction [18]. Comparisons are shown in Fig.5. We employ the 10-th depth of octree in the SSD and Screen-Poisson methods to generate results in Fig.5. For MPU and our method, we adjust the resolutions of polygonization methods to extract meshes with similar numbers of triangles as SSD and Screened-Poisson. The parameter Max_Error of MPU is set as 0.001 times of the model's size. Default values are used for other parameters. From observation, it can be found that geometric details on the original mesh can be well preserved by our method while being smoothed out in some prior methods. Publicly available software, Metro tool [41], is employed to compute the average shape approximation error between the reconstructed surface and the original mesh. A bar chart of errors is given in the upper-right of Fig.5. Our method can always generate more accurate results than SSD and MPU. Meanwhile, our results have similar accuracy comparing to Screened-Poisson.

Table 3 gives the computational statistics of tests on these models. Due to the close-form formulation, our method does not need any global operation such as solving a large linear system. Therefore, its computational time is only spent on constructing an octree to computing the support size and the step of function value evaluation in iso-surface extraction. Both SSD and Screened-Poisson need to solve linear systems globally. In Poisson reconstruction, the multi-grid solver performs a constant number of conjugate-gradient iterations at each level, which gives linear complexity w.r.t to the number of nodes in the octree.

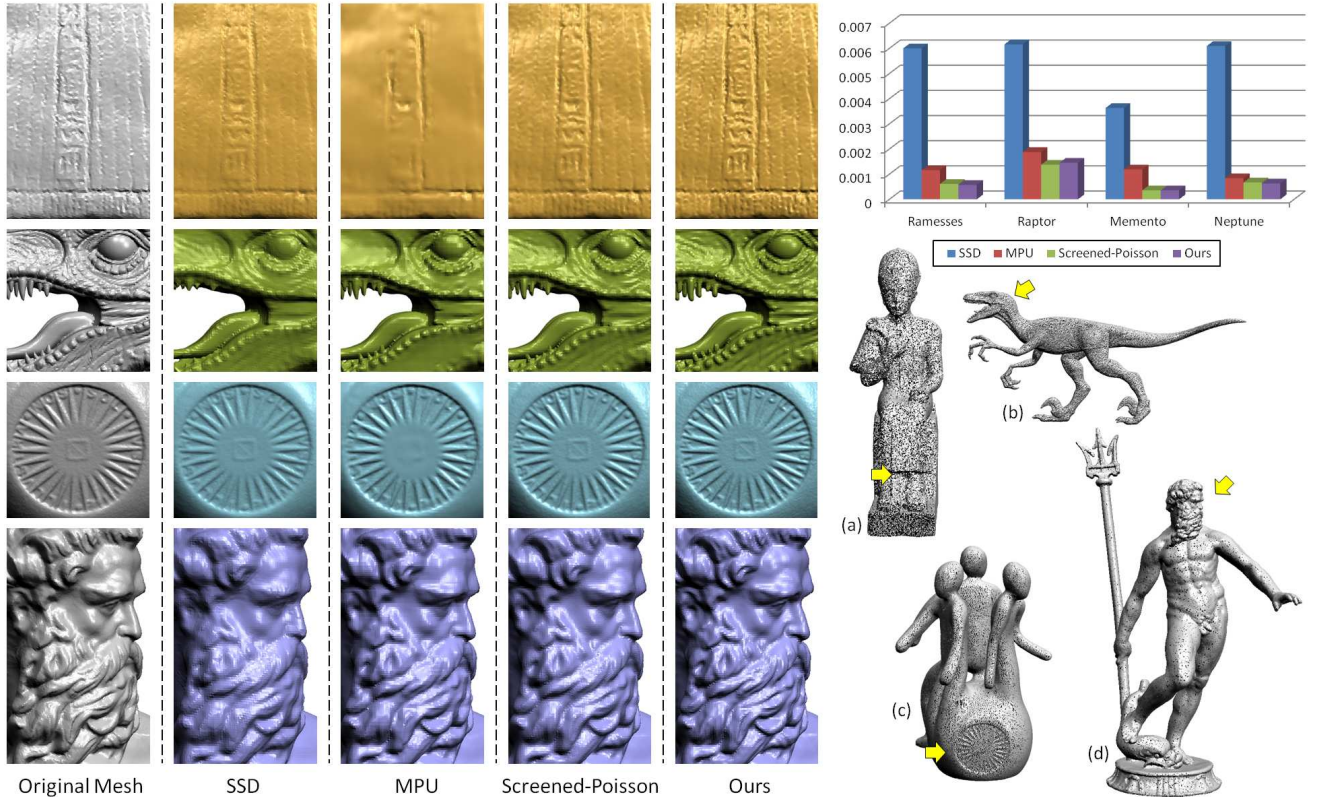


Fig. 5. Experimental tests on clean point cloud that is uniformly sampled from four mesh models – (a) Ramesses (0.580M pts.), (b) Raptor (1.00M pts.), (c) Memento (2.52M pts.) and (d) Neptune (4.98M pts.). For illustration, only 1/10 points are displayed for the points of the first three models, and 1/20 points for the Neptune model. The reconstructions by different methods including SSD, MPU, Screened-Poisson and ours are shown and compared in the left. A bar chart is also given to report the average shape approximation errors on different reconstructions by the Metro tool [41]. We use $s\bar{d} = 0.003$ as the support size and $w = 0.001$ for the grid width of polygonization in all examples here. To conduct a fair comparison, similar number of triangles are generated through the polygonization for different approaches.

The SSD reconstruction uses conjugate-gradients to determine all the coefficients simultaneously, which has a complexity of $O(n^{1.5})$. This leads to a significantly slower performance on models with large number of points (see Table 3). In MPU reconstruction, only local fitting is taken at leaf-nodes of an octree. These surfaces are blended together to form the resultant surface, which is fast but still slower than ours. Moreover, our method generates results with smaller shape approximation error than MPU (see Fig.5). In summary, our method is the fastest method and can generate similar results as the best of other three in terms of quality.

5.2 Raw data

In practice, the real data obtained from an acquisition process are usually large and noisy point sets. Meanwhile, the data sets are incomplete in most cases (e.g., the Aquarius and the Horse models shown in Fig.6). The recently developed FSSR method [5] is targeting on fast surface reconstruction from such kind of real data. We compare our method with FSSR

TABLE 3
Runtime performance of different reconstruction approaches on clean point sets[†]

Model	Pts.	Time in Seconds*			
		SSD	MPU	Poisson	Ours
Ramesses	0.58M	14,314	61.2	40.8	8.3
Raptor	1.00M	1,799	47.2	31.6	6.8
Memento	2.52M	24,195	138.8	92.6	20.4
Neptune	4.98M	6,772	139.4	114.0	18.9

*Note that, the time reported here includes both the surface reconstruction and the mesh extraction.

[†]To have a fair comparison, similar number of triangles are generated for different approaches.

on two sets of real scanned data in Fig.6. Fuhrmann and Goesele [5] assumed the *scale* of an input point set is known, which however is not the case here. Although it can be computed by using the average distance to k -nearest neighbors, it is difficult to set a proper k for reconstructing a smooth surface. In order to make an appropriate comparison, we use 1/3 of the average support size determined by our method

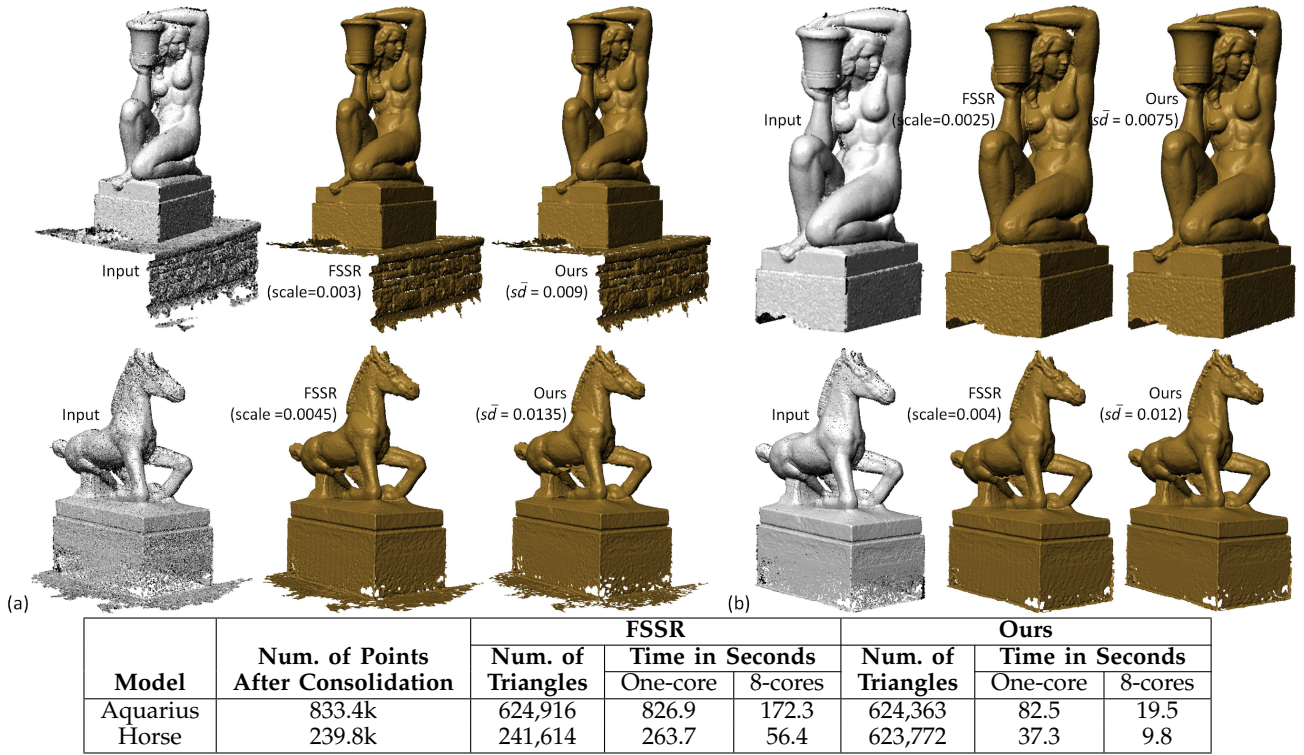


Fig. 6. Examples of surface reconstruction on incomplete set of points: (a) reconstruction from raw data and (b) reconstruction from data sets processed by the consolidation method [42]. Our results are comparable with that obtained by FSSR but ours is $5.76\times \sim 10.0\times$ faster.

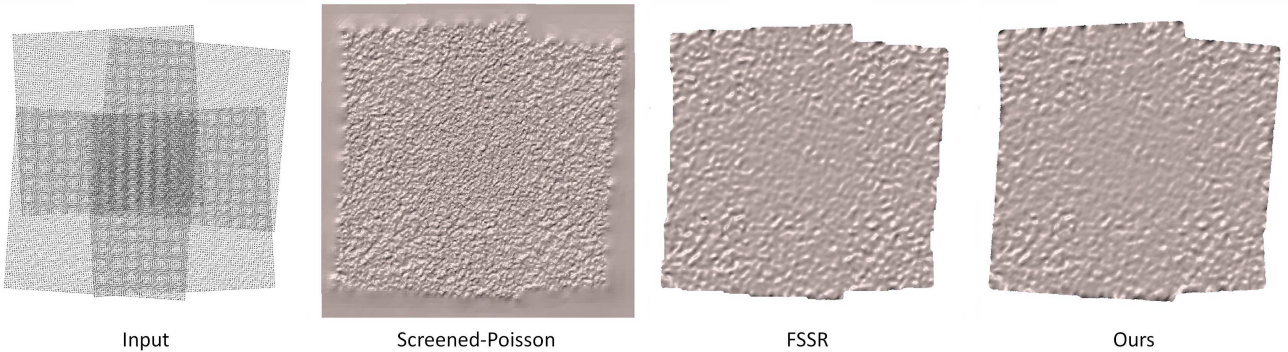


Fig. 7. When processing an input with significant density variation – e.g., from four synthetic scans (most-left), FSSR and ours can avoid generating unwanted artifacts caused by high frequency noises. The total time of our reconstruction is 6.81 sec. ($s = 3.0$ and 342k triangles are obtained on the resultant mesh), while FSSR takes 670 sec. and results in 301k triangles (scale=0.0105). Both are tested on a CPU with eight-cores.

as the scale used in FSSR. This is consistent with the formulation presented in [5], where the support size is set as three times of the input scale. The actual values of scale and $s\bar{d}$ are also given in Fig.6. It can be found that similar number of triangles are generated in FSSR and our method by setting the value of scale in this way. Note that, as both FSSR and ours do not need any global operations during the computation of surface reconstruction, it can easily be parallelized on the PC with multi-cores – OpenMP is used in our implementation. We test both approaches on a PC with 8-cores. As shown in the computational statistics in Fig.6, the program can be effectively speed up on

8-cores. The multi-core version of FSSR is provided by the authors on their homepage.

We also study the effectiveness of our approach on the benchmark of FSSR with shape density variation caused by superposing point sets obtained from multiple scans. As shown in Fig.7, the input set from four synthetic scans is downloaded from the homepage of FSSR’s authors. Our reconstruction is similar to the result from FSSR but ours method is much faster.

5.3 Verification of numerical error

Error bound of the quasi-solution $\tilde{\lambda}$ obtained by our closed-form formulation with reference to the exact

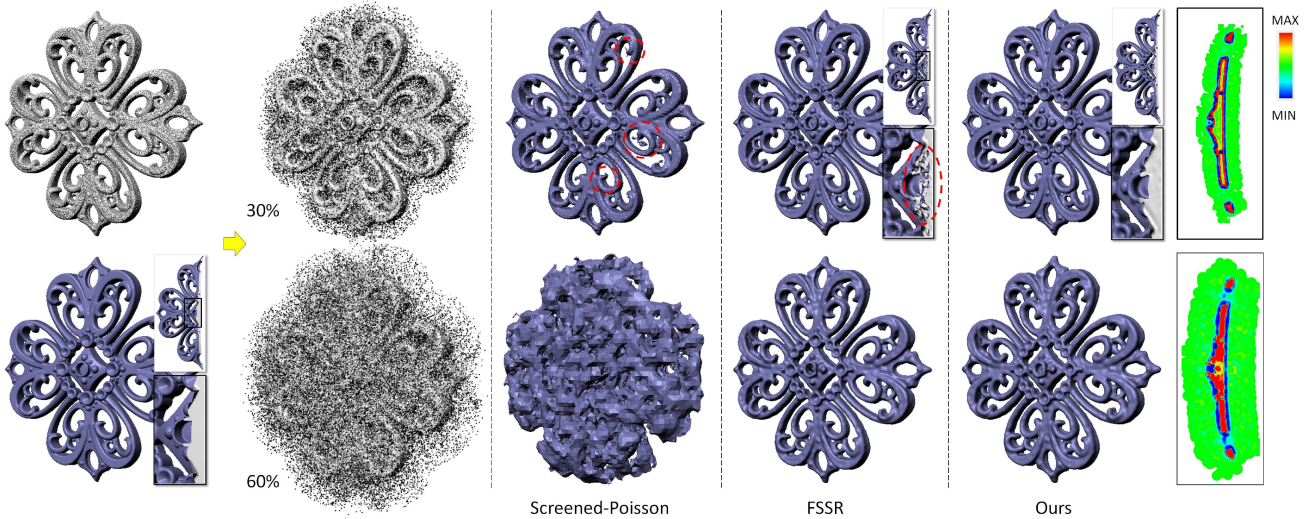


Fig. 8. Examples of reconstruction from sets (having 250k points) with different level of Gaussian noises. Topological errors can be found on the results of Screen-Poisson and FSSR (see the regions circled by dashed lines in red). The cross-sectional view of function values in our reconstruction has also been given in the right, where the regions in white color have undefined function values.

TABLE 4
Error Statistics of Quasi-Solution

Model	Figure	η	$\ \tilde{\lambda} - \lambda\ _{\infty}$
Ramesses	5(a)	457,616	9.52×10^{-8}
Raptor	5(b)	1,666,700	1.98×10^{-8}
Aquarius	6(a)	176,771	3.46×10^{-7}
Horse	6(a)	149,459	3.47×10^{-7}

solution λ of Eq.(7) has been derived in Section 3.2. It is also interesting to study the error between $\tilde{\lambda}$ and λ . We measure $\|\tilde{\lambda} - \lambda\|_{\infty}$ in examples shown above and the results are listed in Table 4.

From the statistics, it can be easily found that our quasi-solution provides very accurate results on both the clean point cloud and the real data. The numerical solver for computing the exact solution runs out of memory on the two examples – Momento and Neptune in Fig.5. Thus, the errors cannot be evaluated and shown here.

5.4 Noisy data

In the following tests, we verify the robustness of our approach on input with noises at different levels. For a given point set \mathcal{P} with normal vectors \mathcal{N} , if the diagonal length of its bounding box is d , a new point set with $\delta\%$ Gaussian noises is obtained as follows:

- $n_G = \lceil \frac{\delta}{100} n_P \rceil$ points are selected from \mathcal{P} into a sub-set \mathcal{G} with n_P denoting the number of points in \mathcal{P} ;
- Randomly generate a set of scale with Gaussian distribution, $\mathcal{D}_G = \{d_i\}$, $i = 1, 2, \dots, n_G$, with $d_i \in [0, \delta d/1000]$;
- Impose the noises onto the points in \mathcal{G} by $\mathbf{p}'_j = \mathbf{p}_j + d_j \mathbf{n}_j$ for all $\mathbf{p}_j \in \mathcal{G}$.

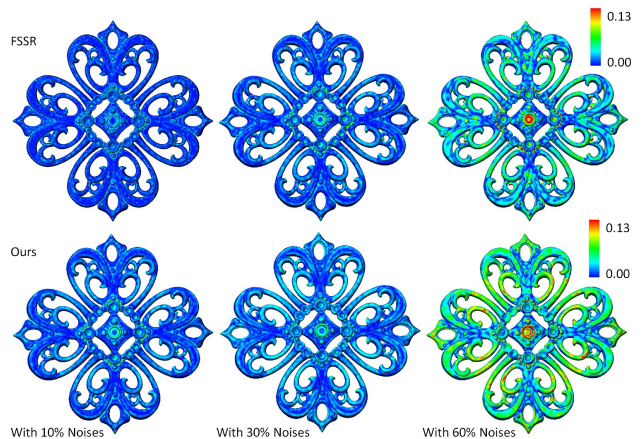


Fig. 9. Color maps to visualize the forward-distance based errors on the results generated by FSSR (top row) and our method (bottom row).

Normal vectors on a set of noisy points are re-generated by the orientation-aware *Principal Component Analysis* (PCA) with p -nearest neighbors – here $p = 6$ is used in all tests.

We reconstruct mesh surfaces from a filigree model with 30% and 60% Gaussian noises by different methods, including Screen-Poisson, FSSR and ours (see Fig.8). The noise-free set of points are sampled from a mesh model so that we can compare the results of reconstruction with the original mesh to evaluate the shape approximate errors generated by different method. Screen-Poisson reconstruction does not perform well on noisy model. As shown in Fig.8, models with incorrect topology are generated. FSSR and ours can still reconstruct ‘correct’ models even after embedding 60% Gaussian noises. We then compare these two methods in terms of shape approximation error by

TABLE 5
Error Statistics of Reconstruction on Noisy Input

FSSR on the Filigree Model (Fig.8)					
Noisy Level	Forward Dist.		Backward Dist.		Scale
	Max.	Ave.	Max.	Ave.	
10%	.00360	.000295	.0175	.00315	.00375
30%	.00800	.00600	.0325	.0014	.00670
60%	.0115	.00145	.0300	.00170	.0112

Our Method on the Filigree Model (Fig.8)					
Noisy Level	Forward Dist.		Backward Dist.		s
	Max.	Ave.	Max.	Ave.	
10%	.00405	.000255	.0115	.000275	1.9
30%	.00700	.000800	.00700	.000800	2.7
60%	.0135	.00210	.0150	.00220	3.5

*The errors are measured by the Metro tool [41].

the Metro tool [41] (see Table 5). In the measurements based on forward distances from ground-truth to the reconstruction, FSSR has slightly smaller errors (see also the visualization in Fig.9). In the errors based on backward distances (i.e., from reconstruction to ground-truth), our method outperforms FSSR. This is because FSSR generates some interior isolated regions (i.e., topological errors) but our method does not – see the zoom-view in Fig.8. Moreover, our method is $17.5\times$ and $36.4\times$ faster than FSSR on the 30% and 60% noisy models respectively.

5.5 Limitation

The limitations of our approach are mainly caused by the nature of locally compact support of kernel functions. As a result, we share the following common limitations as the FSSR method.

- Near the boundary of regions with function-value defined, some small fragments isolated from the main reconstruction could be formed by the numerical oscillation. Such isolated fragments must be removed by the post-processing step taken on the mesh surface after polygonization.
- Although reconstruction with high quality can be found at the example shown in Fig.7, misaligned multiple scan could lead to multi-layers of points, therefore also have multiple surface layers produced at those ‘overlapped’ regions.

Caused by these limitations, when a set of points with low quality (e.g., the set obtained from two Kinect sensors as shown in Fig.10) are used as input, neither FSSR nor ours can obtain water-tight surface as generated by Screen-Poisson reconstruction.

6 CONCLUSION

In this paper, we present a novel surface reconstruction method based on computing an approximate solution of HRBF-based implicit surface fitting. The approximate solution is formulated as a weighted sum of compactly supported basis functions centered

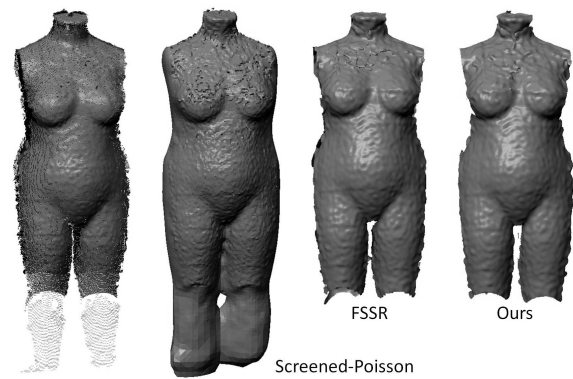


Fig. 10. For an input point set (left most) with low quality from Kinect, all methods generate poor results.

at input data points equipped with normal vectors (i.e., we provide a closed-form solution without any global operation). The implicit function for surface reconstruction can be efficiently and robustly evaluated. The error-bound between our approximate solution and the exact solution has been derived, which can be guaranteed as long as the maximum number of points covered in the supports of RBF kernels is capped by a fixed number. Moreover, to strengthen the performance of our approach on input with high non-uniformity, a center selection algorithm has also been introduced. Experimental results have shown the performance of our approach by comparing to the state-of-the-arts.

No global operation needs to be applied during the surface reconstruction of our approach. As a result, it is easy to extend our implementation to run in the out-of-core manner or on a distributed PC-cluster. We would like to further investigate the strength of our method in this aspect in our future work, which can make it possible to realize the on-site reconstruction of large-scale 3D models (e.g., outdoor scenes like city scale). Many robotics and virtual reality applications could benefit from this work.

ACKNOWLEDGMENTS

The authors would like to thank the support provided by the HKSAR RGC General Research Fund (CUHK/14207414) and the Natural Science Foundation of China (Ref. No.: 61173119).

REFERENCES

- [1] J. Carr, R. Beatson, J. Cherrie, T. Mitchell, W. Fright, B. McCallum, and T. Evans, “Reconstruction and representation of 3d objects with radial basis function,” in *Proceedings of ACM SIGGRAPH 2001*, 2001, pp. 67–76.
- [2] G. Turk and J. F. O’Brien, “Modeling with implicit surfaces that interpolate,” *ACM Transactions on Graphics*, vol. 21, no. 4, pp. 855–873, 2002.
- [3] H. Wendland, *Scattered data approximation*. Cambridge: Cambridge University Press, 2005.
- [4] I. Macedo, J. P. Gois, and L. Velho, “Hermite radial basis functions implicit,” *Computer Graphics Forum*, vol. 30, no. 1, pp. 27–42, 2011.

- [5] S. Fuhrmann and M. Goesele, "Floating scale surface reconstruction," *ACM Trans. Graph.*, vol. 33, no. 4, pp. 46:1–46:11, 2014.
- [6] M. Berger, J. A. Levine, L. G. Nonato, G. Taubin, and C. T. Silva, "A benchmark for surface reconstruction," *ACM Trans. Graph.*, vol. 32, no. 2, pp. 20:1–20:17, 2013.
- [7] H. Hoppe, T. DeRose, T. Duchamp, J. McDonald, and W. Stuetzle, "Surface reconstruction from unorganized points," in *Proceedings of ACM SIGGRAPH 1992*, 1992, pp. 71–78.
- [8] B. Morse, T. Yoo, P. Rheingans, D. Chen, and K. Subramanian, "Interpolating implicit surfaces from scattered surfaces data using compactly supported radial basis functions," in *Shape Modeling International 2001*, May 2001, pp. 89–98.
- [9] Y. Ohtake, A. Belyaev, and H. Seidel, "3D scattered data interpolation and approximation with multilevel compactly supported RBFs," *Graphical Models*, vol. 67, pp. 150–165, 2005.
- [10] R. Pan, X. Meng, and T. Whangbo, "Hermite variational implicit surface reconstruction," *Science in China Series F: Information Sciences*, vol. 52, no. 2, pp. 308–315, 2009.
- [11] M. Samozino, M. Alexa, P. Alliez, and M. Yvinec, "Reconstruction with voronoi centered radial basis functions," in *Proceeding SGP '06 Proceedings of the fourth Eurographics symposium on Geometry processing*, 2006, pp. 51–60.
- [12] J. Sussmuth, Q. Meyer, and G. Greiner, "Surface reconstruction based on hierarchical floating radial basis functions," *Computer Graphics Forum*, vol. 29, no. 6, pp. 1854–1864, 2010.
- [13] Y. Ohtake, A. Belyaev, and H. Seidel, "Sparse surface reconstruction with adaptive partition of unity and radial basis functions," *Graphical Models*, vol. 68, no. 1, pp. 15–24, 2006.
- [14] I. Tobor, P. Reuter, and C. Schlick, "Reconstructing multi-scale variational partition of unity implicit surfaces with attributes," *Graphical Models*, vol. 68, no. 1, pp. 25–41, 2006.
- [15] C. Walder, B. Schölkopf, and O. Chapelle, "Implicit surface modeling with a globally regularised basis of compact support," *Computer Graphics Forum*, vol. 25, no. 3, pp. 635–644, 2006.
- [16] P. Alliez, D. Cohen-Steiner, Y. Tong, and M. Desbrun, "Voronoi-based variational reconstruction of unoriented point sets," in *Proceedings of Symposium on Geometry Processing*, 2007, pp. 39–48.
- [17] M. Kazhdan, M. Bolitho, and H. Hoppe, "Poisson surface reconstruction," in *Proceedings of Symposium on Geometry Processing*, 2006, pp. 61–70.
- [18] M. Kazhdan and H. Hoppe, "Screened poisson surface reconstruction," *ACM Transactions on Graphics*, 2013.
- [19] F. Calakli and G. Taubin, "SSD: Smooth signed distance surface reconstruction," *Computer Graphics Forum*, vol. 30, no. 7, pp. 493–501, 2011.
- [20] M. Alexa, J. Behr, D. Cohen-Or, S. Fleishman, D. Levin, and C. Silva, "Point set surfaces," in *Proceedings of the conference on Visualization'01*, 2001, pp. 21–28.
- [21] G. Guennebaud and M. Gross, "Algebraic point set surface," in *Proceedings of ACM Siggraph 2007*, 2007, pp. 23.1–23.9.
- [22] N. Amenta and Y. Kil, "Defining point-set surfaces," *ACM Transactions on Graphics*, vol. 23, no. 3, pp. 264–270, 2004.
- [23] C. Oztireli, G. Guennebaud, and M. Gross, "Feature preserving point set surfaces based on non-linear kernel regression," *Computer Graphics Forum*, vol. 28, no. 2, pp. 493–501, 2009.
- [24] M. Alexa and A. Adamson, "Interpolatory point set surfaces-convexity and hermite data," *ACM Transactions on Graphics*, vol. 28, no. 2, p. No.20, 2009.
- [25] P. Yang and X. Qian, "Direct boolean intersection between acquired and designed geometry," *Computer-Aided Design*, vol. 41, no. 2, pp. 81–94, 2009.
- [26] J. Manson, G. Petrova, and S. Schaefer, "Streaming surface reconstruction using wavelets," in *Proceedings of the Symposium on Geometry Processing*, 2008, pp. 1411–1420.
- [27] J. P. Gois, V. Polizelli-Junior, T. Etienne, E. Tejada, A. Castelo, L. G. Nonato, and T. Ertl, "Twofold adaptive partition of unity implicits," *The Visual Computer*, vol. 24, no. 12, pp. 1013–1023, 2008.
- [28] Y. Ohtake, A. Belyaev, M. Alexa, G. Turk, and H. Seidel, "Multi-level partition of unity implicits," *ACM Transaction on Graphics*, vol. 22, no. 3, pp. 463–470, 2003.
- [29] D. Shepard, "A two-dimensional interpolation function for irregularly-spaced data," in *Proceedings of the 1968 ACM National Conference*, 1968, pp. 517–524.
- [30] H. Xie, K. T. McDonnell, and H. Qin, "Surface reconstruction of noisy and defective data sets," in *Proceedings of the Conference on Visualization '04*, 2004, pp. 259–266.
- [31] M. Buhmann, "On quasi-interpolation with radial basis functions," *Journal of Approximation Theory*, vol. 72, no. 1, pp. 103–130, 1993.
- [32] Z. Wu and Z. Xiong, "Multivariate quasi-interpolation in $l^p(r^d)$ with radial basis functions for scattered data," *International Journal of Computer Mathematics*, vol. 87, no. 3, pp. 583–590, 2010.
- [33] X. Han and M. Hou, "Quasi-interpolation for data fitting by the radial basis functions," in *GMP'08: Proceedings of Geometric Modeling and Processing*, 2008, pp. 541–547.
- [34] S. Liu and C. Wang, "Quasi-interpolation for surface reconstruction from scattered data with radial basis functions," *Computer Aided Geometric Design*, vol. 29, no. 7, pp. 435–447, 2012.
- [35] H. Wendland, "Piecewise polynomial, positive definite and compactly supported radial basis functions of minimal degree," *Advances in Computational Mathematics*, vol. 4, pp. 389–396, 1995.
- [36] H. Q. Dinh, G. Turk, and G. Slabaugh, "Reconstructing surfaces by volumetric regularization using radial basis functions," *IEEE Trans. Pattern Anal. Mach. Intell.*, vol. 24, no. 10, pp. 1358–1371, 2002.
- [37] W. E. Lorensen and H. E. Cline, "Marching cubes: A high resolution 3d surface construction algorithm," *Computer Graphics*, vol. 21, no. 4, pp. 163–169, 1987.
- [38] T. Ju, F. Losasso, S. Schaefer, and J. Warren, "Dual contouring of hermite data," in *Proceedings of ACM SIGGRAPH 2002*, 2002, pp. 339–346.
- [39] C. C. L. Wang, "Approximate boolean operations on large polyhedral solids with partial mesh reconstruction," *IEEE Transactions on Visualization and Computer Graphics*, vol. 17, no. 6, pp. 836–849, 2011.
- [40] S. J. Liu and C. C. L. Wang, "Orienting unorganized points for surface reconstruction," *Computers & Graphics*, vol. 34, no. 3, pp. 209–218, 2010.
- [41] P. Cignoni, C. Rocchini, and R. Scopigno, "Metro: measuring error on simplified surfaces," *Computer Graphics Forum*, vol. 17, no. 2, pp. 167–174, 1998.
- [42] J. Wang, K. Xu, L. Liu, J. Cao, S. Liu, Z. Yu, and X. D. Gu, "Consolidation of low-quality point clouds from outdoor scenes," *Comput. Graph. Forum*, vol. 32, no. 5, pp. 207–216, 2013.